A material model to reproduce mixed-mode fracture in concrete

F. Suárez[a], J.C. Gálvez[b], D.A. Cendón[c]

[a]*Departamento de Ingeniería Mecánica y Minera. Universidad de Jaén. Campus Científico-Tecnológico de Linares. Cinturón Sur 23700-Linares (Jaén)*
[b]*Departamento de Ingeniería Civil- Construcción. Universidad Politécnica de Madrid . E.T.S.I. Caminos, Canales y Puertos, C/ Profesor Aranguren s/n 28040 – Madrid, Spain*
[c]*Departamento de Ciencia de Materiales, Universidad Politécnica de Madrid . E.T.S.I. Caminos, Canales y Puertos, C/ Profesor Aranguren s/n 28040 – Madrid, Spain*

Abstract

This paper presents a material model to reproduce crack propagation in cement-based material specimens under mixed-mode loading. Its numerical formulation is based on the cohesive crack model, proposed by Hillerborg, and extended for the mixed-mode case. This model is inspired by former works by Gálvez et al., but implemented for its use in a finite element code at a material level, that is to say, at an integration point level. Among its main features, the model is able to predict the crack orientation and can reproduce the fracture behaviour under mixed-mode fracture loading. In addition, several experimental results found in the literature are properly reproduced by the model.

Keywords: Mixed-mode fracture, Material model, Finite element method, Cement-based materials

*F. Suárez
Email address: `fsuarez@ujaen.es` (F. Suárez)

Nomenclature

$\boldsymbol{\sigma}_{e,n}$	Elastic estimation of the stress tensor at step n
$\Delta\boldsymbol{\sigma}_{e,n}$	Elastic increment of the stress tensor at step n
$\Delta\boldsymbol{\sigma}_{i,n}$	Inelastic increment of the stress tensor at step n
$\boldsymbol{\varepsilon}_n$	Strain tensor at step n
$\boldsymbol{E}$	Elastic tangent tensor
$\boldsymbol{D}_n$	Elastic-plastic tangent tensor at step n
$\Delta\boldsymbol{\varepsilon}_n$	Increment of the strain tensor at step n
$\boldsymbol{t}_n^i$	Stress vector for step n at iteration i
σ_n^i	Normal-to-the-crack component of stress vector $\boldsymbol{t}$ for step n at iteration i
τ_n^i	Tangent-to-the-crack component of stress vector $\boldsymbol{t}$ for step n at iteration i
α	Crack angle, with 0^o being the horizontal direction
u_n^i	Crack process driving parameter for step n at iteration i
$\Delta\lambda_i$	Inelastic corrector at iteration i
f_{t0}	Material tensile strength
$f_{t,n}^i$	Tensile strength for step n at iteration i
c_0	Material cohesion
c_n^i	Cohesion for step n at iteration i
G_{F_I}	Fracture energy for mode I
$G_{F_{II}}$	Fracture energy for mode II
l_{ch}	Finite element characteristic length
$G_{F_I}^*$	Fracture energy for mode I corrected at an integration point level
$G_{F_{II}^*}$	Fracture energy for mode II corrected at an integration point level
ϕ_f	Friction angle of the material; it remains constant for the whole fracture process
ϕ_d	Dilatancy angle
$\phi_{d,max}$	Maximum dilatancy angle
$u_{cri,dil}$	Value of u for which ϕ_d becomes null
F	Failure criterion for mixed-mode loading
$\boldsymbol{n}$	Perpendicular-to-the-cracking-surface unit vector
$\boldsymbol{m}$	Parallel-to-the-cracking-surface unit vector
Q_n^i	Plastic potential for step n at iteration i
$\boldsymbol{L}$	Change-of-base matrix between xy and st coordinates

1. Introduction

Reproducing fracture by numerical methods has attracted a high number of researchers in the last decades. Quasi-brittle materials, such as concrete, count with a high number of numerical models and different approaches that are well known and have been studied in depth for many years.[1,2] The concept of *cohesive crack* was introduced by Dugdale[3] and Barenblatt[4] in the early sixties, but it was Hillerborg[5] who implemented it in a more practical way; since then, this concept has been used in many occasions.

With regard of those based on the Finite Element Method (FEM), they are traditionally classified into three groups: smeared crack, discrete crack and lattice approaches. In the smeared crack approach, fracture is reproduced by modifying the strain field, adding up a nonlinear strain that corresponds to the fracture process and accordingly decreasing the material stiffness.[6] This approach appeared in the sixties[7] and has developed over the years, introducing some interesting features, such as the rotating crack.[8] The discrete crack approach includes a crack with a certain direction and opening inside an element;[9,10] this can be done by using interface elements[11,12] or embedding the crack inside the finite elements mesh.[13,14,15,16] The lattice approach replaces the continuum media by a lattice or a truss[17] and has been successfully applied to concrete-like materials.[18,19]

As already mentioned, the cohesive crack model has been widely used with quasi-brittle materials, such as concrete and cement. It has proved to be successful in many situations where mode I is dominant, such as crack opening in a symmetric three point-bending test. Modelling fracture of this type of materials by means of a fracture model has several advantages, since it is simple and easy to calibrate, given that it is fed with parameters that can be obtained by standardised tests.[20,21]

Nevertheless, there are occasions where fracture is driven by a combination of mode I and mode II, the so-called mixed-mode fracture case. This has been studied experimentally by a number of researchers. The first attempts were based on the tests on double-V notched metallic specimens by Iosipescu,[22] some of them can be consulted in.[23,24,25,26,27,28] Other interesting results can also be found in[29] and,[30] although the latter tests polymethyl methacrylate specimens.

Regarding the numerical simulation of mixed-mode fracture processes, the models by García-Álvarez et al.[31,32] and Cendón and Gálvez[33,11,34] present an interesting approach. In both cases, fracture is modelled by interface elements that reproduce the cohesive behaviour defined by Hillerborg, but introducing variations to take into account the interaction of mode I and mode II.

The present paper is inspired by the work by Gálvez et al.[11] In that case, the fracture was developed by means of interface elements, therefore, the crack path should be known *a priori*, so that the finite element mesh had the interface elements placed in the correct position and correctly oriented. This was achieved by means of a pre-process that, using the *Maximum Tangential Direction* (MTS) criterion,[35] provided the crack path using the fundamentals of the Linear Elastic Fracture Mechanics (LEFM).

The main objective in this work is to provide a tool that predicts the crack propagation under mixed-mode loading on concrete-like materials without providing the crack path as an input. To do this, the fracture behaviour is based on the work described in,[11] which uses the hyperbolic expression proposed by Červenka[10] to consider the interaction of modes I and II, but formulated at a material level. This is done by predicting the crack orientation at an integration point level and developing the corresponding continuum mechanics behaviour to provide the needed values by the FEM under an implicit time integration, that is to say, the stress tensor $\boldsymbol{\sigma}$ and the material tangent tensor $\boldsymbol{D}$.

In the following sections, firstly the material model behaviour is described and later its implementation into the FEM code Abaqus® detailed. Finally, the model is validated by reproducing several experimental tests that are available in the literature.

2. Description of the fracture model

In this section the developed mixed-mode fracture model is presented. To do so, the classical cohesive crack model is briefly described, which is successful for reproducing mode I fracture cases. Then the extension of this concept to a mixed-mode fracture case combining mode I and mode II is explained, based on the main ideas developed by Gálvez et al.[33,11,34] In their work, mixed-mode fracture in concrete was reproduced by means of interface elements that simulated the crack opening. Therefore, the crack path should be known *a priori*, for which linear elastic fracture mechanics (LEFM) was used; in practice, the finite element code FRAN2D[36] was utilised for predicting the crack path. Here the approach is different and the crack path is computed for each integration point by an algorithm that rotates crack around the integration point and finds the crack orientation, based on a failure criterion formulated by Červenka.[10]

2.1. Cohesive crack

The cohesive crack model was developed in 1976 by Hillerborg et al.,[5] who generalised the work by Dugdale and Barenblatt[3,4] by defining a Fracture Process Zone at the crack tip that only propagates when the tensile stress equals a critical value f_{t0}. Once this value is reached, the cohesive stress progressively decreases as the crack opens (Figure 1). Therefore, the cohesive strength σ and the crack opening w are related by means of a function, usually referred to as *softening curve*. This function is basically defined by only two parameters, the tensile strength f_{t0} and the fracture energy G_F. The former is, as mentioned before, the stress at which the crack starts to open and propagate, the latter can be seen as the area below the softening curve. Both of them are material properties and can be obtained by standadised tests.[20,21]

The choice of the shape of the softening function is quite open, for example, in the case of concrete, Hillerborg proposed a linear function and, later, Petersson a bilinear one.[37] Since then, the bilinear definition of the softening curve was accepted as a good approximation for concrete, a material for which fracture has been often numerically reproduced by cohesive models. Later, the softening curve has been defined by exponential functions,[38,39,40] which has two main advantages with respect to the bilinear function: it only requires two parameters to be defined (f_t, G_F) and its derivative is continuous, which is very convenient for the numerical implementation of the model.[41]

For a deep review on this model, the reader is referred to.[1]

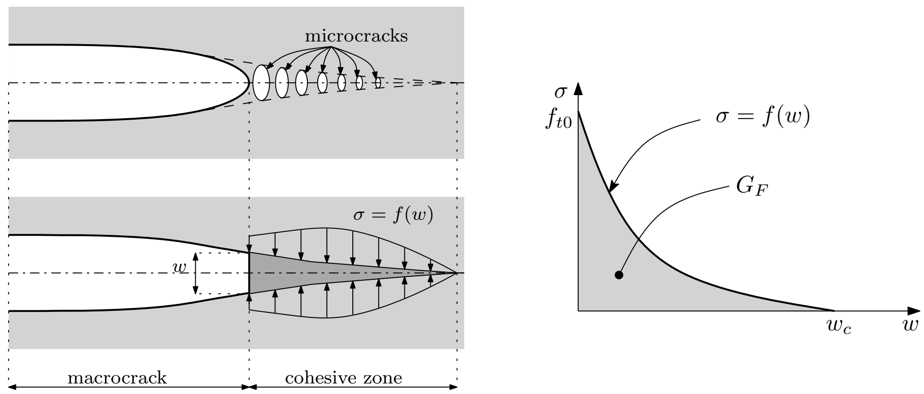

Figure 1: Cohesive crack in a three point bending test and the corresponding material softening curve.

2.2. *Cohesive crack under mixed-mode loading*

Here, the main ingredients of the model are presented. Note that during the fracture process, some values evolve and this will be guided by a crack-process-driving parameter called u. As will later be discussed, the evolution of this driving parameter modifies the fracture behaviour by changing the values of several parameters, namely the tensile strength f_t (related to mode I crack opening), the cohesion c and the dilatancy angle ϕ_d (both related to mode II crack opening); these details will be treated later.

2.2.1. *Failure criterion*

In the case of the cohesive crack model, cracking process evolves only depending on the tensile stress. In mixed-mode fracture, the interaction between normal stress σ and tangential stress τ is taken into account by means of a failure function that defines a cracking surface on the $\sigma - \tau$ plane. The expression considered here is the hyperbolic expression proposed by Červenka,[10] which is based on the previous work by Carol et al.:[42]

$$F = \tau^2 - 2 \cdot c \cdot \tan \phi_f \cdot (f_t - \sigma) - \tan^2 \phi_f \cdot \left(\sigma^2 - f_t^2\right) \tag{1}$$

where τ stands for the tangential stress, c for the material cohesion, ϕ_f denotes the friction angle and f_t the tensile strength; these parameters evolve as damage accumulates. According to this criterion, the material is under linear elastic regime if $F < 0$ and failure develops when $F = 0$.

Therefore, the failure criterion is expressed in terms of the intrinsic components of the stress vector $\boldsymbol{t}$, which can be defined as the summation of a normal component and a tangential component:

$$\boldsymbol{t} = \sigma \cdot \boldsymbol{n} + \tau \cdot \boldsymbol{m} \tag{2}$$

where $\boldsymbol{n}$ and $\boldsymbol{m}$ are the unit vectors perpendicular and parallel to the crack surface (Figure 2).

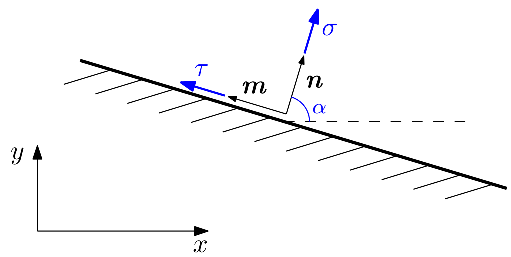

Figure 2: Vectors $\boldsymbol{n}$ and $\boldsymbol{m}$ are the unit vectors normal and perpendicular to the crack orientation, respectively.

2.2.2. Softening curves for tensile strength and cohesion

For the evolution of both, tensile strength f_t and cohesion c, exponential expressions of the softening curves are used. Differently from the work by Gálvez et al.,[11] the approach here is defined at a material level. The fracture problem developed in their work, by which the present work is inspired, is described in terms of crack opening and applied forces for an interface element. Given that now the problem is described at a material level, the traction-separation law must be expressed in terms of a stress-strain law, which can be achieved by setting the cracking strain equal to the crack opening divided by a length value representing the width of the band of finite elements in which crack localises.[43] In this case, this is done by dividing the fracture energy of mode I, G_{F_I}, by the characteristic length of the element, l_{ch}, which for a planar model is defined as the square root of the element area. The fracture energies adapted for usage at a material level will be denoted as $G^*_{F_I}$ and $G^*_{F_{II}}$:

$$G^*_{FI} = \frac{G_{F_I}}{l_{ch}} \tag{3}$$

The fracture energy of mode II, $G_{F_{II}}$, is defined as a function of G_{F_I} in order to avoid numerical issues in the iterative process that will be described later, therefore, the fracture energies defined at a material level are related as follows:

$$G^*_{F_{II}} = \frac{c_0}{f_{t0}} G^*_{F_I} \tag{4}$$

Therefore, parameters f_t and c are defined by the following exponential functions:

$$f_t = f_{t0} \cdot \exp\left(-\frac{u \cdot f_{t0}}{G^*_{F_I}}\right) \tag{5}$$

$$c = c_0 \cdot \exp\left(-\frac{u \cdot c_0}{G^*_{F_{II}}}\right) = c_0 \cdot \exp\left(-\frac{u \cdot f_{t0}}{G^*_{F_I}}\right) \tag{6}$$

where u is a cumulative damage parameter that will be defined later.

2.2.3. Dilatancy

In cohesive-frictional materials such as concrete, the effect of dilatancy must be taken into account.[44,45,46] Due to the irregular geometry of the crack surface, once a tangential slipping is applied (mode II), a normal opening is induced (mode I). This phenomenon forces to relate the incremental inelastic displacements at the crack surface, $\dot{u}_n^i$ and $\dot{u}_t^i$, by means of a dilatancy angle ϕ_d:

$$\tan \phi_d = \frac{\dot{u}_n^i}{\dot{u}_t^i} \tag{7}$$

Given that dilatancy is an effect that depends on the roughness of the crack surface, it diminishes as the surface is more damaged and the crack lips are more apart.

In classical plasticity, the direction of the inelastic deformation is known as *flow rule* and is perpendicular to the plastic potential ($Q = constant$). In the same spirit, the incremental inelastic displacement is expressed as:

$$\dot{\boldsymbol{u}}^i = \dot{\lambda} \frac{\partial Q(\boldsymbol{t})}{\partial \boldsymbol{t}} = \dot{\lambda} \boldsymbol{b} \tag{8}$$

where Q stands for the plastic potential, $\dot{\lambda}$ the incremental inelastic corrector and $\boldsymbol{b}$ the direction vector normal to the plastic potential.

Here, the dilatancy is considered to vary linearly with the damage driving parameter u, becoming zero value for a critical value called $u_{cri,dil}$:

$$\phi_d = \begin{cases} \phi_{d,max} \left(1 - \frac{u}{u_{cri,dil}}\right) & \forall\ u < u_{cri,dil} \\ 0 & \forall\ u \geq u_{cri,dil} \end{cases} \tag{9}$$

where $\phi_{d,max}$ is the maximum dilatancy angle.

2.2.4. Damage evolution under mixed-mode loading

As mentioned before, the fracture process is driven by a parameter u that, as it can be observed, affects the values of f_t, c and ϕ_d. Since the failure criterion expressed by (1) depends on these values, we can say that the value of u defines the hyperbolic fracture surface on the $\sigma - \tau$ plane.

For what comes next, it is important to note that there will be two planes of work: a) the geometrical plane where everything will be referred to axes xy and the stress state will be represented by the stress tensor $\boldsymbol{\sigma}$ expressed in this coordinate system and b) a stress plane $\sigma - \tau$ that will represent the stress state of the material in terms of normal and tangential stresses referred to a certain crack orientation.

Let us say that at a certain n step, the crack angle α (see Figure 2), the stress vector $\boldsymbol{t}_n$ and the damage driving parameter u are known; then, for the next step, an increment of strain $\Delta\boldsymbol{\varepsilon}_{n+1}$ takes place. The stress increment at the end of the step will be computed as the combination of an elastic estimation minus an inelastic corrector:

$$\Delta\boldsymbol{\sigma}_{n+1} = \Delta\boldsymbol{\sigma}_{e,n+1} - \Delta\boldsymbol{\sigma}_{i,n+1} \tag{10}$$

The elastic part is easily obtained by means of the elastic tangent tensor $\boldsymbol{E}$:

$$\Delta\boldsymbol{\sigma}_{e,n+1} = \boldsymbol{E} \cdot \Delta\boldsymbol{\varepsilon}_{n+1} \tag{11}$$

The expression of $\boldsymbol{E}$ for a plane stress case is:

$$\boldsymbol{E} = \frac{E}{1-\nu^2}\begin{pmatrix} 1 & \nu & 0 \\ \nu & 1 & 0 \\ 0 & 0 & \frac{1-\nu}{2} \end{pmatrix} \tag{12}$$

To determine the inelastic corrector, an iterative process will be carried out on the $\sigma - \tau$ plane, since the fracture criterion (1) is postulated in those terms. Therefore, the elastic increment is expressed in terms of $\sigma - \tau$ by means of Cauchy's lemma:

$$\Delta\boldsymbol{t}_{e,n+1} = \Delta\boldsymbol{\sigma}_{e,n+1} \cdot \boldsymbol{n} \tag{13}$$

where $\boldsymbol{n}$ is the unit vector normal to the crack orientation (α corresponds to the inclination angle of $\boldsymbol{n}$):

$$\boldsymbol{n} = \begin{pmatrix} \cos\alpha \\ \sin\alpha \end{pmatrix} \tag{14}$$

Then, the elastic estimation of the increment of $\boldsymbol{t}$ can be obtained as:

$$\boldsymbol{t}_{e,n+1} = \boldsymbol{t}_n + \Delta\boldsymbol{t}_{e,n+1} \tag{15}$$

Figure 3 shows how the following iterative process is applied, here subscripts stand for the step number and superscripts for the iteration number in the current step. Up to this point, an elastic prediction of $\boldsymbol{t}$ is known, $(\sigma^0_{n+1}, \tau^0_{n+1})$, which does not meet the failure criterion, since it is out of the failure surface $F_n(\sigma, \tau)$. Then, a first iteration is carried out by applying an inelastic correction $\Delta\lambda$ that finds a solution on the failure surface:

$$\boldsymbol{t}^1_{n+1} = \boldsymbol{t}_{e,n+1} - \Delta\lambda^1 \cdot \boldsymbol{E} \cdot \boldsymbol{b}_n \tag{16}$$

Note that $\boldsymbol{b}$ defines the orientation of the inelastic correction on the $\sigma - \tau$ plane (due to the effect of dilatancy) and corresponds to step n; this is just a way to start the iterative process, since there is no known $\boldsymbol{b}$ vector for this step.

Once the value of the inelastic corrector is obtained for this first iteration, $\Delta\lambda^1$, all the variables included in the failure criterion are updated:

$$u^1_{n+1} = u_n + \Delta\lambda^1 \tag{17}$$

With this new value of the driver u and with the resulting stress vector $\boldsymbol{t}^1_{n+1}$, the failure criterion is not satisfied anymore (it met this condition for the previous value of u, but not for the updated one), thus a new iteration is needed, so f_t, c and ϕ_d (thus, $\boldsymbol{b}$) are computed again and the new $\boldsymbol{t}_{n+1}$ obtained for the corresponding hyperbolic fracture surface. This process continues until the inelastic corrector is small enough:

$$
\begin{aligned}
\boldsymbol{t}^1_{n+1} = \quad & \boldsymbol{t}_{e,n+1} - \Delta\lambda^1 \cdot \boldsymbol{E} \cdot \boldsymbol{b}^1 \\
& \downarrow \text{Obtain } \Delta\lambda^1 \Rightarrow u^1 = u_n + \Delta\lambda^1 \\
\boldsymbol{t}^2_{n+1} = \quad & \boldsymbol{t}^1_{n+1} - \Delta\lambda^2 \cdot \boldsymbol{E} \cdot \boldsymbol{b}^2 \\
& \downarrow \text{Obtain } \Delta\lambda^2 \Rightarrow u^2 = u^1 + \Delta\lambda^2 \\
\boldsymbol{t}^3_{n+1} = \quad & \boldsymbol{t}^2_{n+1} - \Delta\lambda^3 \cdot \boldsymbol{E} \cdot \boldsymbol{b}^3 \\
& \downarrow \text{Obtain } \Delta\lambda^3 \Rightarrow u^3 = u^2 + \Delta\lambda^3 \\
& \vdots \text{ Until } \Delta\lambda^i \text{ is small enough}
\end{aligned}
$$

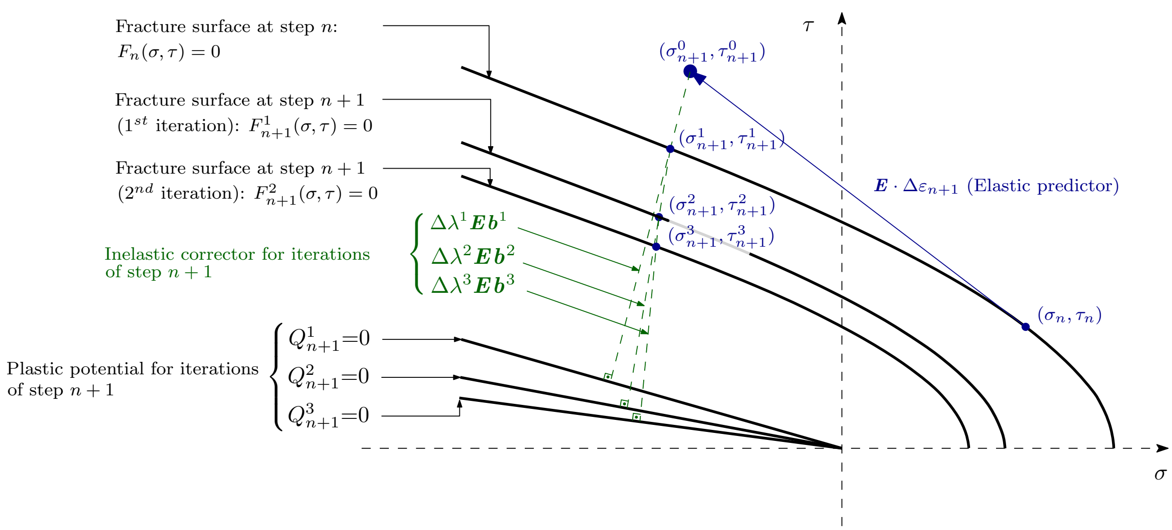

Figure 3: Graphical description of the iterative process that finds the stress vector $\boldsymbol{t}$ for a given strain increment $\Delta\boldsymbol{\varepsilon}$.

At the end of this process, the final components of $\boldsymbol{t}_{n+1}$ are obtained.

Then, according to,[11] the tangent tensor can be computed by means of:

$$
\boldsymbol{C}^{ep} = \boldsymbol{E} - \frac{\boldsymbol{E}\,(\boldsymbol{b}\otimes\boldsymbol{a})\,\boldsymbol{E}}{\boldsymbol{a}\cdot\boldsymbol{E}\boldsymbol{b} - \dfrac{\partial F}{\partial u}|\boldsymbol{b}|} \tag{18}
$$

where $\boldsymbol{b}$ is, in practice, the return direction to the cracking surface at the end of the iterative process, and $\boldsymbol{a}$ the derivative of F with respect to $\boldsymbol{t}$:

$$
\boldsymbol{b} = \frac{\partial Q}{\partial \boldsymbol{t}} \qquad \boldsymbol{a} = \frac{\partial F}{\partial \boldsymbol{t}}
$$

In (18), product $\otimes$ stands for the direct product which in the Einstein's notation can be expressed as:

$$(b \otimes a)_{i,j} = a_i \cdot b_j \tag{19}$$

2.3. Crack initiation and orientation

Since the model is formulated at a material level, there is no information *a priori* of the crack orientation, therefore, one of the main tasks consists of its computation. Here the process is explained and the criterion for initiating the crack and setting its orientation.

Let us say that at a certain step the material is still intact and no damage has been developed. Under a certain strain increment, damage may be induced, but with what orientation? The orientation is defined by α, which corresponds to the angle between the x axis direction and the normal-to-the-crack unit vector $\boldsymbol{n}$ (see Fig. 2). Therefore, each value of this parameter defines a possible fracture plane. By means of Cauchy's lemma, the stress vector $\boldsymbol{t}$ can be computed for a certain value of α, thus the failure criterion (1) can be checked. If $F \leq 0$, then damage does not develop and if $F \geq 0$, it does develop. By simply computing this for values of α in the range $[0, \pi]$, the planes at which failure can develop are identified.

Nevertheless, there may be several values of α for which the failure criterion is satisfied, but only one must be selected. Here, the criterion is based on the distance to the hyperbola defined by (1). Therefore, for each value of α that satisfies the failure criterion, the distance from its corresponding $(\sigma_\alpha, \tau_\alpha)$ point in the $\sigma - \tau$ plane to the hyperbola defined by (1) is computed. The value of α for which the failure criterion is satisfied and the distance is maximum is selected as the crack orientation. For example, Figure 4 shows a case where four values of α provide four points at the $\sigma - \tau$ plane. Point 1 is inside the hyperbola, therefore the evaluation of F would result into a negative value, which means that damage does not develop. Points 2 to 4 are outside the hyperbola, which means that $F \geq 0$ and, therefore, damage may initiate for any of the associated values of α. Based only on these four points, the aforementioned criterion would result in the selection of point 3, since it presents a higher value of its distance to the hyperbola. It is also interesting to mention that, as described before, dilatancy allows defining the incremental variation of the inelastic correction of $\boldsymbol{t}$, which in practice is interpreted as the return vector $\boldsymbol{b}$. Carefully observing the figure, it is clear that for points 2 and 3, the definition of $\boldsymbol{b}$ is easy and equal, but when the normal stress σ is predominant with respect to the tangential stress τ (which is the case of point 4), the plastic potential ($Q = \textit{constant}$) is not defined. As the figure shows, here the return direction to the origin ($\sigma = \tau = 0$) is adopted.

3. Implementation in a FEM code

The model has been implemented in the commercial code Abaqus®[47] using its implicit version by means of a UMAT user subroutine.Therefore, the model

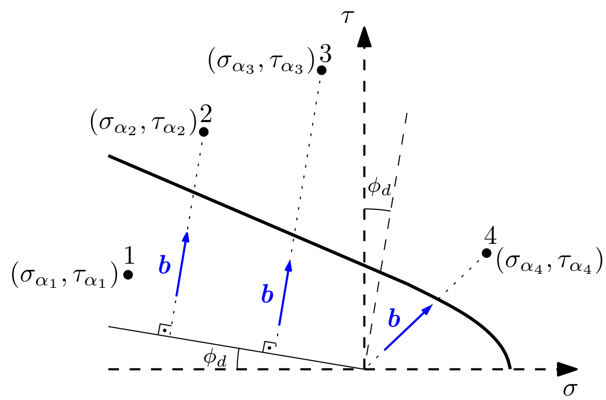

Figure 4: Election of α depending on the corresponding distance to the hyperbola defined by F.

is run at each integration point of each element and, since the Newton-Raphson method is applied, both the stress tensor and the tangent tensor must be defined.

Figure 5 shows the general scheme of the model implemented with a UMAT user subroutine. The material model receives the increment of the strain tensor for the current step $n+1$, $\Delta\boldsymbol{\varepsilon}_{n+1}$, as input and must provide the stress tensor, $\boldsymbol{\sigma}_{n+1}$, and the tangent tensor, $\boldsymbol{D}_{n+1}$. Depending on the history of the material at each integration point, this will be done following different procedures.

Firstly, if the material is not intact and has already experienced damage in the past, $\boldsymbol{\sigma}_{n+1}$ and $\boldsymbol{D}_{n+1}$ are computed using a procedure referred to as *algorithm 1*, which will be explained later. On the contrary, if the material has not experienced damage, an elastic prediction of the stress tensor is obtained by simply operating the elastic tensor $\boldsymbol{E}$ with the total strain computed as the summation of the strain in the previous step and the increment received as input:

$$\boldsymbol{\sigma}_{n+1} = \boldsymbol{E} \cdot (\boldsymbol{\varepsilon}_n + \Delta\boldsymbol{\varepsilon}_{n+1})$$

Then, the resulting stress tensor is evaluated for each value of α in the range $[0, \pi]$ by the procedure called *algorithm 2*, which has been detailed in section 2.3. If the failure criterion defined by (1) is lower or equal than 0 for any value of α, then damage does not occur in this step and the material response is elastic. If, on the contrary, *algorithm 2* returns a specific value of α for which damage evolves in this step, $\boldsymbol{\sigma}_{n+1}$ and $\boldsymbol{D}_{n+1}$ are obtained by means of *algorithm 1*.

3.1. Definition of $\boldsymbol{\sigma}_{n+1}$ and $\boldsymbol{D}_{n+1}$ in the case of increasing damage

Given that, as previously mentioned, the model works in two spaces: the xy plane and the $\sigma - \tau$ plane, it is necessary to change from one base to another in the procedure that follows. Let us call $\boldsymbol{L}$ to the change-of-base matrix that allows coming from the $\sigma - \tau$ plane to the xy plane. The procedure can be described as follows:

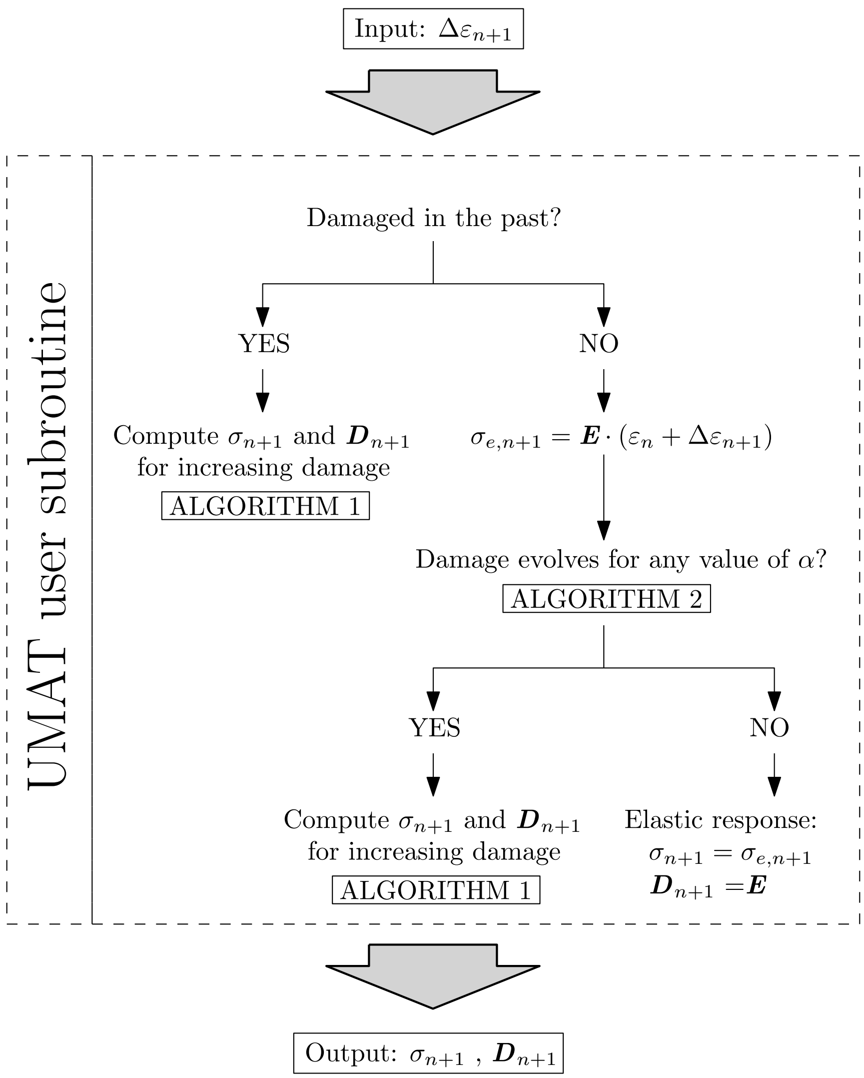

Figure 5: General scheme of the model behaviour.

1. The elastic prediction of the increment of $\boldsymbol{\sigma}$ is obtained: $\Delta\boldsymbol{\sigma}_{e,n+1} = \boldsymbol{E} \cdot \Delta\boldsymbol{\varepsilon}_{n+1}$.
2. The elastic increment expressed in the $\sigma - \tau$ plane can be computed by means of Cauchy's lemma: $\Delta\boldsymbol{t}_{e,n+1} = \Delta\boldsymbol{\sigma}_{e,n+1} \cdot \boldsymbol{n}$.
3. The starting point for the iterative process described in Figure 3 is defined by: $\boldsymbol{t}_{e,n+1} = \boldsymbol{t}_n + \Delta\boldsymbol{t}_{e,n+1}$.
4. Using a Newton-Raphson iterative process, the inelastic corrector $\Delta\lambda$ can be obtained as described in section 2.2.4. Resulting from this process, $\boldsymbol{t}_{n+1}$ is obtained.
5. The increment of (σ, τ) is computed: $\boldsymbol{\Delta} t_{n+1} = \boldsymbol{t}_{n+1} - \boldsymbol{t}_n$, which can be expressed in the form of a matrix:

$$\Delta\boldsymbol{t}_{n+1} = \begin{pmatrix} \Delta\sigma & \Delta\tau \\ \Delta\tau & 0 \end{pmatrix}$$

6. By simply applying the change-of-base matrix $\boldsymbol{L}$, the increment of the stress tensor can be computed:

$$\Delta\boldsymbol{\sigma}_{n+1} = \boldsymbol{L} \cdot \Delta\boldsymbol{t}_{n+1} \cdot \boldsymbol{L}^T$$

7. Therefore: $\boldsymbol{\sigma}_{n+1} = \boldsymbol{\sigma}_n + \boldsymbol{\Delta\sigma}_{n+1}$.
8. Finally, the tangent tensor is computed using the expression (18). Such expression is applied in the $\sigma - \tau$, Appendix A provides the expression to obtain its form in the xy plane.

4. Experimental validation of the model

In order to validate the material model, five tests are numerically reproduced. Since it is capable of dealing with combinations of mode I and mode II fracture cases, the following tests are considered:

- Predominant mode I: classical three-point-bending test on notched specimen.
- Combination of modes I and II: three-point-bending test on notched specimen with non-symmetric boundary conditions (to be described in detail later). Two cases will be analysed.
- Predominant mode II: pull-out test for anchor bolts embedded in concrete. Two variations of this test will be reproduced.

It must be noted that, since some tests are compared with works where no infomation on some of the paramaters that are needed to feed the model, such as c, ϕ_f and ϕ_d, these values are estimated based on the values used in,[10] which are considered as appropriate for concrete.

4.1. Three-point-bending test on notched specimen

The classical three-point-bending test, usually employed for finding the fracture parameters in quasibrittle materials[21] is reproduced according to the case analysed by Sancho et al.[15] The dimensions of the specimen can be found in Figure 6a.

Material properties are defined with the following values: tensile strength $f_{t0} = 2.5$ MPa, elastic modulus 20 GPa, Poisson's ratio 0.15, mode I fracture energy 100 N/m and cohesion 5 MPa, friction angle $\phi_f = 50^o$ and maximum dilatancy angle $\phi_{d,max} = 50^o$.

When the model is run, it can predict the correct crack path easily, but once the crack progresses up to a certain point, the model is not able to converge and the computation stops. As de Borst et al. point out,[48] this is probably due to the fact that at some point there are several equilibrium states and the iterative solution process finds different solutions at each iteration, leading to a non-convergent solution. In order to obtain a more developed load-displacement diagram, the model has been run again but defining as damagable elements only those in the crack-path.

Figure 6b shows the deformed meshes used in both cases: with no additional information about the crack-path and defining damagable elements only in the crack-path.

Figure 6c shows the load-displacement of the load point curves, compared with the result obtained by Sancho et al.,[15] which resulted from using the smeared-tip method described in.[1]

In order to study the mesh-size dependence of the formulation and check whether the element characteristic length helps to make the softening curve independent of the element size (see eq. (3)), three models have been prepared. Figure 6d shows the load-displacement curves obtained with meshes of different element sizes in the crack path (10mm , 20mm, and 30 mm in width); in all cases the diagram follows a very similar curve, with slight differences that are not unusual when differente mesh sizes are employed in nonlinear problems.

4.2. Three point bending test on notched specimen with non-symmetric boundary conditions

In[28] an experimental campaign on prismatic notched specimens was carried out performing a variation of the classical three-point bending test. In this case, the load and the supports were not placed symmetrically on the specimen, leading to an inclined crack opening that was induced by a combination of mode I and mode II loading. There are two versions of this test, types 1 and 2; their geometrical features can be observed in Figures 7a and 8a. In fact, type 2 test is not really a three-point bending test, but a four-point one, due to the additional support added on the top surface of the specimen; nevertheless, for the shake of simplicity it has been included here as a variation of the type 1 test.

For both models, material has been defined with the following parameters: tensile strength $f_{t0} = 3$ MPa, elastic modulus 38 GPa, Poisson's ratio 0.2, mode I fracture energy 69 N/m and cohesion 5 MPa, friction angle $\phi_f = 50^o$ and maximum dilatancy angle $\phi_{d,max} = 50^o$.

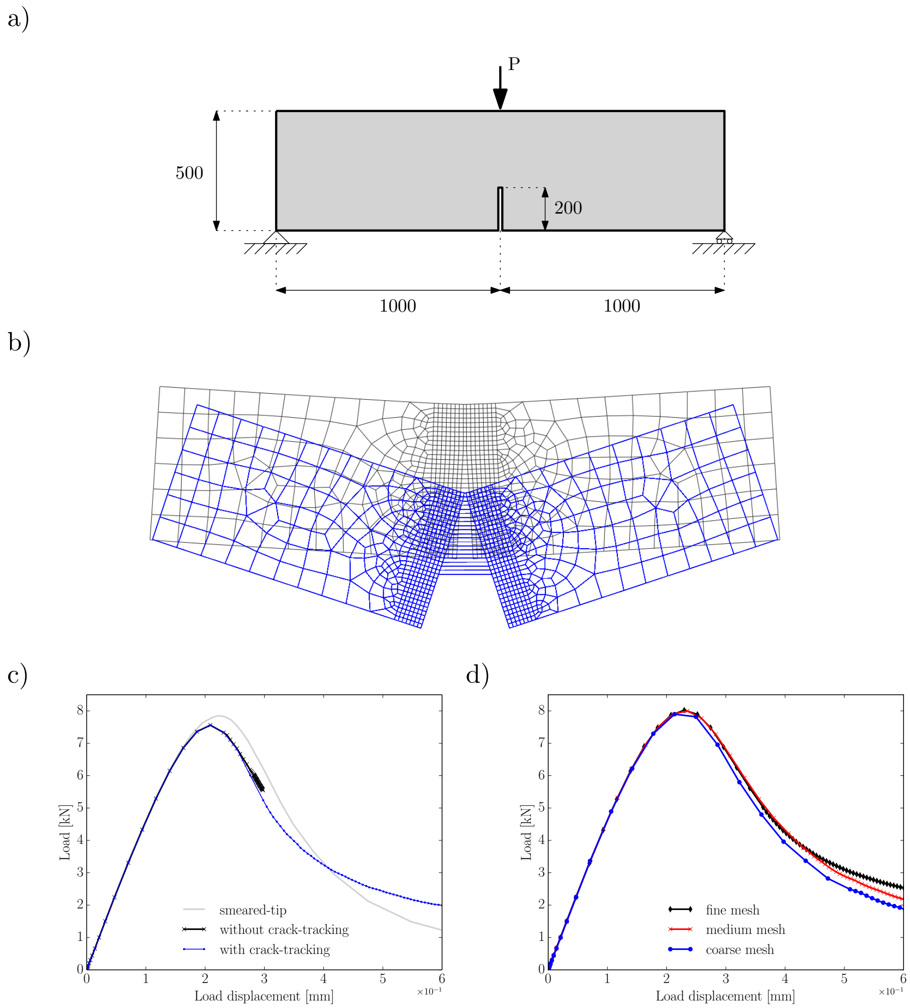

Figure 6: a)Specimen dimensions for the three-point-bending test model expressed in millimetres (thickness = 100 mm.), b)Deformed geometries of the finite element mesh used for modelling the three-point-bending test. In black, the initial model, in blue, the model where only the elements in the crack path could be damaged. Displacements are magnified by a factor of 200, c) Numerical predictions of the model compared with the result by Sancho et al.,[15] obtained by means of the smeared tip method,[1] d) Mesh-size sensitivity analysis

Figure 7b shows the crack orientation compared with the experimental envelope for type 1 test, which proves that the model is able to predict correctly the crack path. Nevertheless, as seen before in the case of a three-point-bending test, here the model could not converge once the crack had progressed up to a certain point. Again, another model has been run where only the elements in the crack path could be damaged. Figure 7c shows the deformed shapes of both models where displacements have been magnified by a factor of 300.

The same modeling work has been carried out for the type 2 test; Figure 8b compares the crack path in the initial model with the experimental envelope and Figure 8c the deformed geometries for both models, one where damage can develop in any element and another one where damage can only develop in those elements crossed by the crack path. The crack again develops in a similar direction as that experimentally observed; obviously, since the model is implemented at a material level with a local formulation, its behaviour presents a clear mesh-dependence. Therefore, as it can be observed in Figure 7b for type 1 test, the mesh forces to some extent the crack evolution; nevertheless, always following a path that is similar to the experimental results.

Finally, Figures 7d, 7e, 8d and 8e present the load-crack mouth opening displacement (CMOD) curves and the load-actuator displacement curves for type 1 and type 2 tests. In both cases, the maximum load is correctly predicted, nevertheless, the behaviour immediately after the post-peak point is, especially in the case of the type 1 test, slightly different, showing a slower load decrease. This behaviour is already known and the response could be improved using finer meshes, as explained in.[49,50,48]

4.3. Pull-out test for anchor bolts embedded in concrete

In order to verify the model under a loading case where fracture develops predominantly under mode II, the results of the round-robin test presented by RILEM Technical Commitee 90-FMA[51,52] are used. In the mentioned round-robin, two different tests are proposed, here, the results obtained by Vervuurt[53,54] for the plane-stress test are used for comparison.

Figure 9a shows the geometry of the model, that takes advantage of the symmetry with respect to the anchor plane, and the corresponding boundary conditions. In the model, the anchor bolt is not included and its pull-out effect is introduced by imposing a vertical displacement on the top contact between the anchor bolt and concrete (boundary b_1 in the figure). Note that only the crack evolution zone is modelled and no lateral constraint is imposed out of it (boundary b_2 in the figure). It is also important to note that there is no contact between concrete and the vertical extension of the bolt, that is why no boundary condition is imposed on that boundary (b_3 in the figure); nevertheless, the anchor bolt is in contact with concrete at the bottom of the vertical steel bar (point p_1 in the figure), that is why this point is horizontally constrained.

Material properties of the model are defined follows: tensile strength $f_{t0} = 3$ MPa,elastic modulus 35 GPa, Poisson's ratio 0.20, mode I fracture energy 100 N/m and cohesion 5 MPa, friction angle $\phi_f = 50^o$ and maximum dilatancy

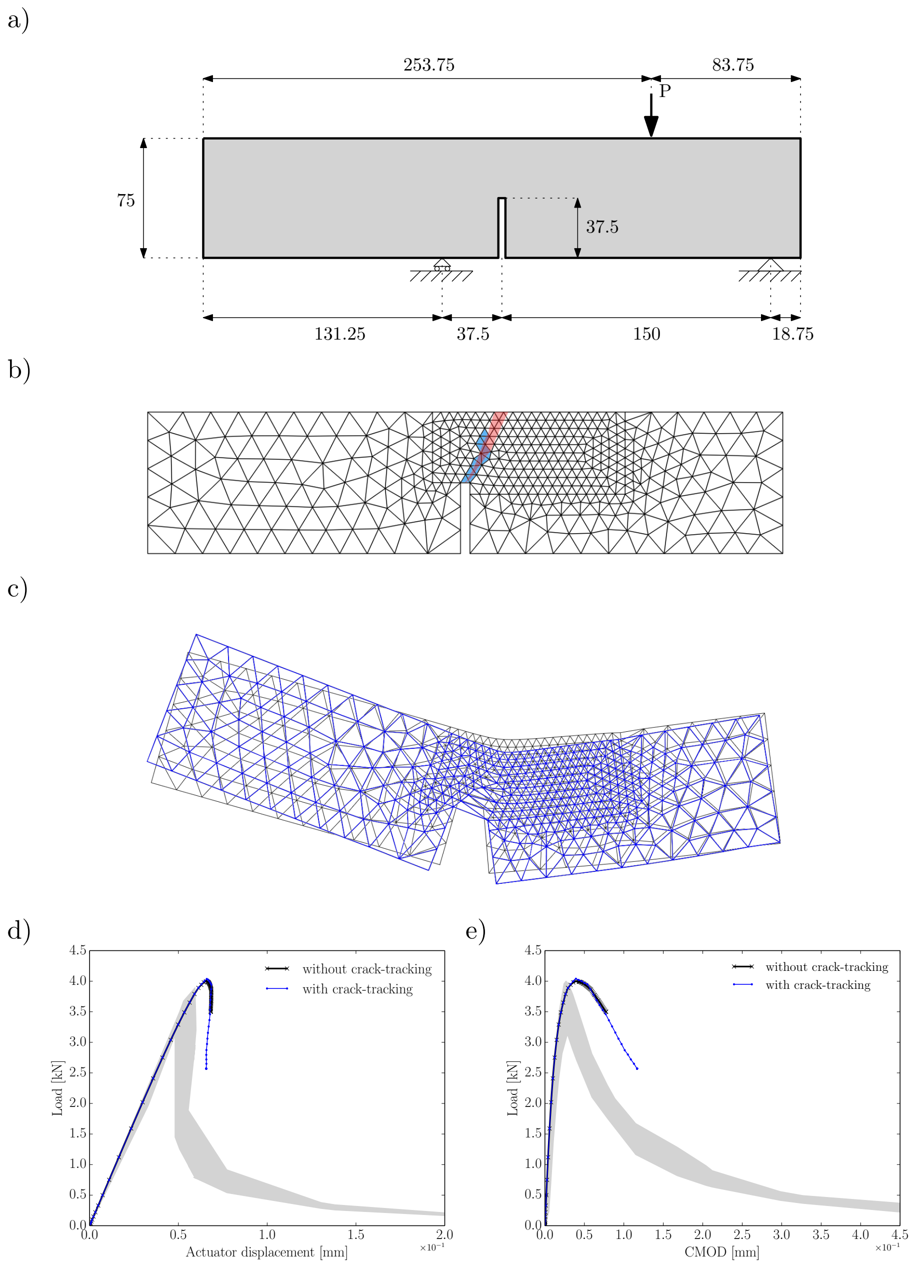

Figure 7: a) Specimen dimensions for the type 1 non-symmetric three-point-bending-test by Gálvez et al.;[28] units in millimetres (thickness = 50 mm.), b) Crack evolution of the model (in blue) compared with the experimental envelope obtained by Gálvez et al.[28] (in red) for the type 1 test, c) Deformed geometries of the finite element mesh used for modelling the type 1 test. In black, the initial model, in blue, the model where only the elements in the crack path could be damaged. Displacements are magnified by a factor of 300, d) Load-actuator displacement diagram of type 1 test with the experimental envelopes obtained in,[28] e) Load-CMOD diagram of type 1 test with the experimental envelopes obtained in.[28]

a)

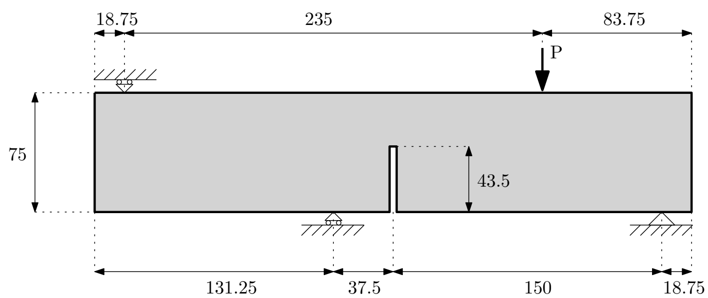

b)

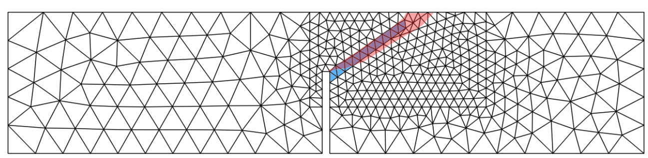

c)

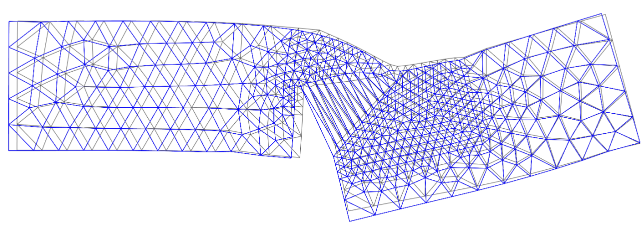

d)

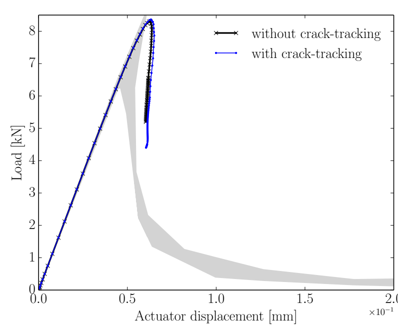

e)

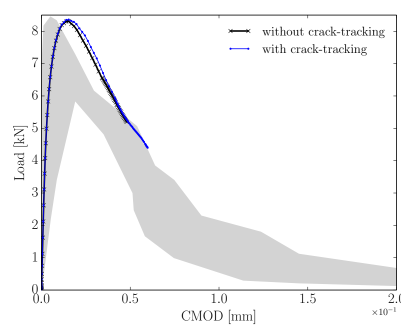

Figure 8: a) Specimen dimensions for the type 2 non-symmetric three-point-bending-test by Gálvez et al.;[28] units in millimetres (thickness = 50 mm.), b) Crack evolution of the model (in blue) compared with the experimental envelope obtained by Gálvez et al.[28] (in red) for the type 2 test, c) Deformed geometry of the finite element mesh used for modelling the type 2 test. In black, the initial model, in blue, the model where only the elements in the crack path could be damaged. Displacements are magnified by a factor of 500, d) Load-actuator displacement diagram of type 2 test with the experimental envelopes obtained in,[28] e) Load-CMOD diagram of type 2 test with the experimental envelopes obtained in.[28]

angle $\phi_{d,max} = 50^o$. Some of these values have been consulted in,[52] others, such as c_0, ϕ_f and $\phi_{d,max}$ have been estimated.

As in the other previous cases, two models have been run, one where all elements are defined with the proposed material model and another one where only those elements in the crack path can be damaged. Figure 9b compares the crack path obtained with the first model with the experimental results obtained by Vervuurt.[53] Figure 9c shows the deformed geometries of the finite element mesh employed in this problem for both cases. The crack path numerically obtained when all elements can be damaged agrees reasonably well with the experimental results if it is reminded that only E, ν, f_{t0} and G_{FI} are available in;[53] the rest of the model parameters have been estimated, but not measured.

The load-displacement diagrams for both models can be observed in Figure 9d. In the first case, the model loses convergence before the maximum load is reached; in the second case damage can progress further and the crack path agrees reasonably well with the experimental result. Regarding the load-displacement diagram, the model seems to predict a stiffer response and an earlier load decrease. It must be noted that it has been fed with parameters found in,[52] but some of them, particularly the elastic modulus and the fracture energy, are not measured values, but estimated; a more precise values of them would probably contribute to a better correlation.

In order to check the ability of the model to reproduce curved crack paths, an additional pull-out model is included. It is inspired by the work presented in,[55] where the plane-stress pull-out test proposed in the RILEM round-robin is reproduced with slightly different boundary conditions respect with those mentioned before (see Figure 9a). The geometry used now is shown in Figure 10a. Apart from the dimensions, which differ from the previous model, the main difference consists of the non-restricted point at the bottom of the vertical boundary in contact with the anchor bolt (point p_1 in the figure) and the constrained horizontal displacement out of the crack-development zone (boundary b_1 in the figure). These differences, as will be observed, result in a very different crack evolution compared with the previous model.

Since the results presented in[55] are not related with standard concrete and its characteristics may not be similar, the model has been developed only to check if it is able to reproduce curved cracking paths. All the elements have been defined as damageable and the material parameters have been equal to those used with the notched specimens tested under a three-point-bending with non-symmetric boundary conditions (see section 4.2).

Figures 10b and 10c show the deformed geometry of the finite element mesh used and the crack path evolution, respectively. As can be observed, the model can predict curved cracking paths, which resemble those obtained by Greco et al. in[55] for lightweight aggregate concrete.

5. Final remarks

A material model to reproduce fracture under mixed-mode loading in cement-based materials is presented. This model is formulated for its implementation

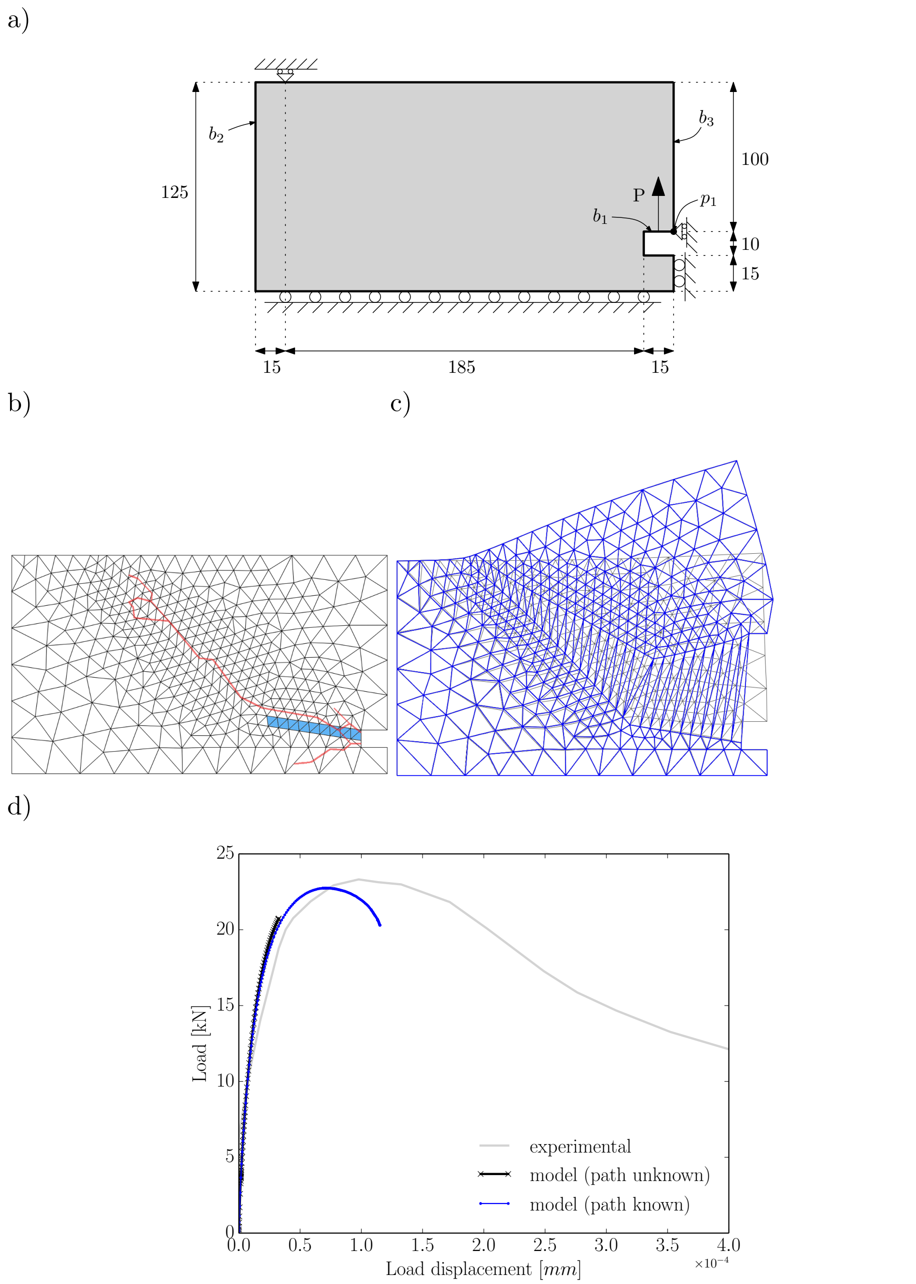

Figure 9: a) Specimen dimensions of the anchor bolt pull-out test performed by Vervuurt et al.;[53] units in millimetres (thickness = 100 mm.), b) Crack evolution of the anchor bolt pull-out model (in blue) that reproduces the results by Vervuurt compared with the experimental observation[53] (in red), c) Deformed geometry of the finite element mesh used for modelling the anchor bolt pull-out test performed by Vervuurt.[53]In black, the initial model, in blue, the model where only the elements in the crack path could be damaged. Displacements are magnified by a factor of 500, d) Load-displacement diagram compared with the experimental result of the anchor bolt pull-out test by Vervuurt.[53]

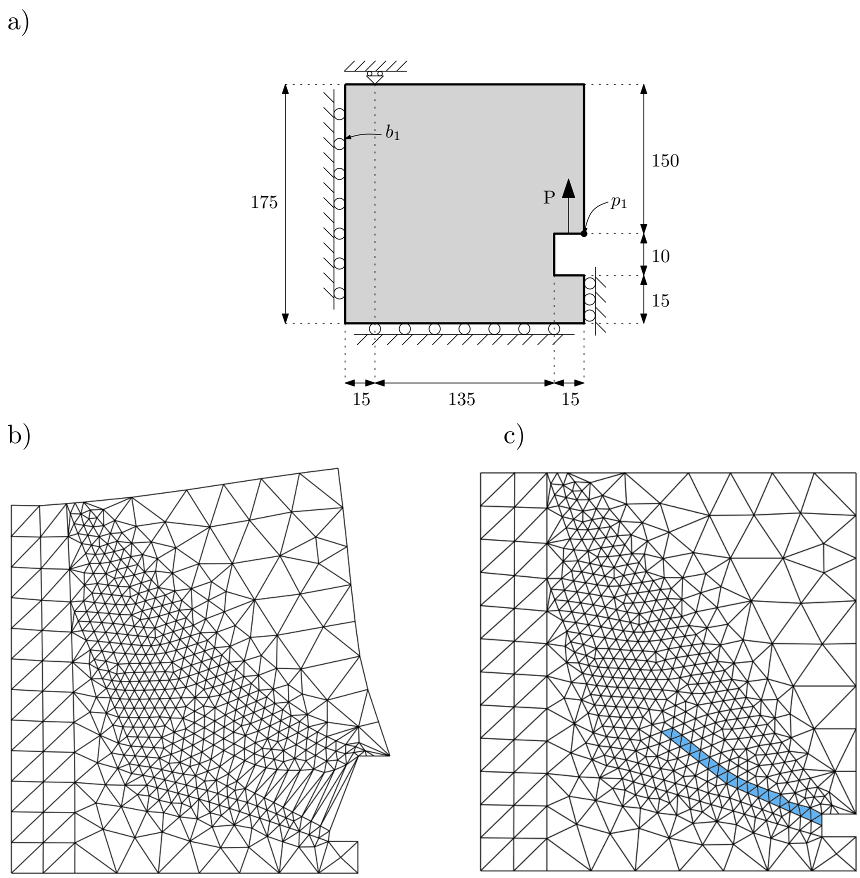

Figure 10: a) Specimen dimensions according to the anchor bolt pull-out test reproduced by Greco et al.;[55] units in millimetres (thickness = 100 mm.), b) Deformed geometry of the finite element mesh; c) Crack evolution in the finite element mesh.

in a FEM code for an integration point, thus, it reproduces the fracture behaviour at a material level. Differently from other works by Gálvez et al., where fracture was modelled by means of interface elements, this model predicts the crack path with no previous pre-processing. To do this, the model initially predicts the crack orientation by applying a failure criterion that takes into account the combination of modes I and II, based on the hyperbolic diagram proposed by Červenka, and, once the crack opening starts, it fixes the crack orientation and reproduces fracture and its corresponding softening process as proposed by Gálvez et al.

It is to be noted that the model only requires a few parameters to determine, some of them easily measurable by standardised tests. Some other parameters, which cannot be obtained experimentally, are estimated based on the recommendations by Červenka.

The model formulation is presented and its implementation in the commercial FEM code Abaqus®, by means of a UMAT user subroutine, explained. It is finally validated with some experimental results found in the literature. More specifically, the works by Sancho et al. are used for a mostly mode I case in a three-point bending test, the works by Gálvez et al. for a combination of mode I and mode II under unsymmetric three-point-bending tests and, finally, some experiments by Vervuurt on anchor bolts pull-out tests for a mostly mode II case.

Although the model is able to predict correctly the crack orientation and reproduce the fracture evolution under several mixed-mode cracking situations, it suffers from mesh-dependence and directional mesh bias; this is not unusual in this type of models and has been extensely documented in the past.[49,50,56] In order to solve these problems several approaches can be adopted, such as using nonlocal models,[57,58,59,60,61] crack-tracking strategies[62,63,64] or even adopting an explicit formulation of the finite element method. Mesh-size dependence has also been studied, verifying that mesh size does not significantly affect the results.

Ackowledgements

The authors gratefully aknowledge the support provided by the Ministry of Economy and Competitiveness of Spain by means of the Research Fund Projects BIA2016-78742-C2-2-R and BIA2014-54916-R.

References

[1] Bazant ZP, Planas J. *Fracture and size effect in concrete and other quasibrittle materials.* CRC press; 1997.

[2] Karihaloo B, Carpinteri A, Elices M. Fracture mechanics of cement mortar and plain concrete. *Adv Cem Based Mater.* 1993;1(2):92–105.

[3] Dugdale DS. Yielding of steel sheets containing slits. *J Mech Phys Solids.* 1960;8(2):100–104.

[4] Barenblatt GI. The Mathematical Theory of Equilibrium Cracks in Brittle Fracture. vol. 7 of *Adv Appl Mech*. Elsevier; 1962. p. 55–129.

[5] Hillerborg A, Modéer M, Petersson PE. Analysis of crack formation and crack growth in concrete by means of fracture mechanics and finite elements. *Cem Concr Res*. 1976;6(6):773 – 781.

[6] Jirásek M. Damage and smeared crack models. *Numerical modeling of concrete cracking*. 2011;p. 1–49.

[7] Rashid Y. Ultimate strength analysis of prestressed concrete pressure vessels. *Nucl Eng Des*. 1968;7(4):334–344.

[8] Jirásek M, Zimmermann T. Rotating crack model with transition to scalar damage. *J Eng Mech-ASCE*. 1998;124(3):277–284.

[9] Jirásek M. Comparative study on finite elements with embedded discontinuities. *Comput Methods in Appl Mech Eng*. 2000;188(1):307–330.

[10] Červenka J. Discrete crack modeling in concrete structures. Doctoral Dissertation. University of Colorado at Boulder; 1994.

[11] Gálvez J, Červenka J, Cendon D, Saouma V. A discrete crack approach to normal/shear cracking of concrete. *Cem Concr Res*. 2002;32(10):1567–1585.

[12] Valente S. On the cohesive crack model in mixed-mode conditions. *Fracture of brittle disordered materials: Concrete, rock and ceramics*. 1995;p. 66–80.

[13] Simo JC, Oliver J, Armero F. An analysis of strong discontinuities induced by strain-softening in rate-independent inelastic solids. *Comput Mech*. 1993;12(5):277–296.

[14] Simo J, Oliver J. A new approach to the analysis and simulation of strong discontinuities. *Fracture and Damage in Quasibrittle Structures*. 1994;p. 25–39.

[15] Sancho JM, Planas J, Cendón DA, Reyes E, Gálvez J. An embedded crack model for finite element analysis of concrete fracture. *Eng Fract Mech*. 2007;74(1):75–86.

[16] Gálvez J, Planas J, Sancho J, Reyes E, Cendón D, Casati M. An embedded cohesive crack model for finite element analysis of quasi-brittle materials. *Eng Fract Mech*. 2013;109:369–386.

[17] Mohammadipour A, Willam K. Lattice approach in continuum and fracture mechanics. *J Appl Mech*. 2016;83(7):071003.

[18] Schlangen E, Van Mier J. Experimental and numerical analysis of micromechanisms of fracture of cement-based composites. *Cement Concrete Comp*. 1992;14(2):105–118.

[19] Schlangen E, Van Mier J. Mixed-mode fracture propagation: a combined numerical and experimental study. *Fracture and damage of concrete and rock*. 1993;p. 166–175.

[20] ASTM C. 496-96. Standard Test Method for Splitting Tensile Strength of Cylindrical Concrete Specimens. 1996;.

[21] RILEM. Determination of the Fracture Energy of Mortar and Concrete by Means of Three-Point Bend Tests on Notched Beams. *Mater Struct*. 1985;18(106):285–290.

[22] Iosipescu N. New accurate procedure for single shear testing of metals. *J Mater*. 1967;2:537–566.

[23] Ingraffea A, Arrea M. Mixed-Mode Crack Propagation in Mortar and Concrete. Dept. of Structural Engineering. Cornell University, USA; 1982.

[24] Bažant Z, Pfeiffer P. Shear fracture tests of concrete. *Mater Struct*. 1986;19(2):111–121.

[25] Biolzi L. Mixed mode fracture in concrete beams. *Eng Fract Mech*. 1990;35(1-3):187–193.

[26] Bocca P, Carpinteri A, Valente S. Mixed mode fracture of concrete. *Int J Solids Struct*. 1991;27(9):1139–1153.

[27] Nooru-Mohamed MB. Mixed-mode fracture of concrete: an experimental approach. Doctoral Dissertation. Delft University of Technology; 1992.

[28] Gálvez J, Elices M, Guinea G, Planas J. Mixed mode fracture of concrete under proportional and nonproportional loading. *Int J Fract*. 1998;94(3):267–284.

[29] Zhao Y. Experimental study on mixed mode crack propagation. *Eng Fract Mech*. 1989;34(4):891–899.

[30] Cooke ML, Pollard DD. Fracture propagation paths under mixed mode loading within rectangular blocks of polymethyl methacrylate. *J Geophys Res Solid Earth*. 1996;101(B2):3387–3400.

[31] García-Álvarez VO, Gettu R, Carol I. Numerical analysis of mixed mode fracture in concrete using interface elements. In: *Proceedings of the European Congress on Computational Methods in Applied Sciences and Engineering*; 2000. .

[32] Garcia-Alvarez VO, Gettu R, Carol I. Analysis of mixed-mode fracture in concrete using interface elements and a cohesive crack model. *Sadhana*. 2012;p. 1–19.

[33] Cendón D, Gálvez J, Elices M, Planas J. Modelling the fracture of concrete under mixed loading. *Int J Fract*. 2000;103(3):293–310.

[34] Gálvez JC, Cendón DA. Simulación de la fractura del hormigón en modo mixto. *Revista internacional de métodos numéricos*. 2002;.

[35] Erdogan F, Sih G. On the crack extension in plates under plane loading and transverse shear. *J Basic Eng-T ASME*. 1963;85(4):519–525.

[36] Wawrzynek P, Ingraffea A. FRANC2D: A two-dimensional crack propagation simulator. Version 2.7: User's guide. 1994;.

[37] Petersson PE. Crack growth and development of fracture zones in plain concrete and similar materials. Doctoral Dissertation. Division of Building Materials, Lund University; 1981.

[38] Gopalaratnam V, Shah SP. Softening response of plain concrete in direct tension. In: *ACI J*. vol. 82. American Concrete Institute; 1985. p. 310–323.

[39] Cornelissen H, Hordijk D, Reinhardt H. Experimental determination of crack softening characteristics of normalweight and lightweight concrete. HERON. 1986;31(2):45–56.

[40] Planas J, Elices M. Towards a measure of GF: an analysis of experimental results. *Fracture toughness and fracture energy of concrete*. 1986;p. 381–390.

[41] Cendón D. Estudio de la fractura en modo mixto de hormigones y morteros. Doctoral Dissertation. Departamento de Ciencia de Materiales, ETS de Ingenieros de Caminos, C. y P., Universidad Politécnica de Madrid; 2002.

[42] Carol I, Bazant ZP, Prat PC. Microplane-type constitutive models for distributed damage and localized cracking in concrete structures. *Proc Fracture Mechanics of Concrete Structures*. 1992;p. 299–304.

[43] Cervera M, Chiumenti M. Smeared crack approach: back to the original track. *Int J Numer Anal Methods Geomech*. 2006;30(12):1173–1199.

[44] Ballarini R, Plesha ME. The effects of crack surface friction and roughness on crack tip stress fields. *Int J Fract*. 1987;34(3):195–207.

[45] Carpinteri A, Scavia C. Energy dissipation due to frictional shake-down on a closed crack subjected to shear. *Meccanica*. 1993;28(4):347–352.

[46] Spagnoli A, Carpinteri A, Terzano M. Near-tip stress fields of rough and frictional cracks under mixed-mode loading. *Fatigue Fract Eng M*. 2018;p. 1–11.

[47] Hibbit H, Karlsson B, Sorensen E. ABAQUS user manual, version 6.12. Simulia, Providence, RI. 2012;.

[48] de Borst R, Crisfield MA, Remmers JJ, Verhoosel CV, et al. *Nonlinear finite element analysis of solids and structures*. John Wiley & Sons; 2012.

[49] Rots JG. Computational modeling of concrete fracture. Doctoral Dissertation. Delft University of Technology; 1988.

[50] Jirásek M, Grassl P. Evaluation of directional mesh bias in concrete fracture simulations using continuum damage models. *Eng Fract Mech.* 2008;75(8):1921–1943.

[51] Elfgren L, Noghabai K. Anchor bolts and tension stiffening of rebars: two RILEM round robin investigations on bond. In: *Proceedings of the International Conference on Fracture Mechanics of Concrete and Concrete Structures: 12/10/1998-16/10/1998*. vol. 2. AEDIFICATIO Publishers; 1998. p. 1279–1290.

[52] Elfgren L, Eligehausen R, Rots J. Anchor bolts in concrete structures: summary of round robin tests and analysis arranged by RILEM TC 90-FMA 'Fracture Mechanics of Concrete-Applications'. *Mater Struct.* 2001;34(8):451–457.

[53] Vervuurt A, van Mier J, Schlangen E. Pull-out of steel anchors embedded in concrete. *Fracture Damage of Concrete and Rock*. 1993;2:569–578.

[54] Vervuurt A, Van Mier JG, Schlangen E. Analyses of anchor pull-out in concrete. *Mater Struct.* 1994;27(5):251–259.

[55] Greco F, Leonetti L, Luciano R. A multiscale model for the numerical simulation of the anchor bolt pull-out test in lightweight aggregate concrete. Constr Build Mater. 2015;95:860–874.

[56] Li F, Xingwen D. Mesh-dependence of Material with Softening Behavior. *Chin J Aeronaut.* 2010;23(1):46 – 53.

[57] Bažant ZP. Nonlocal damage theory based on micromechanics of crack interactions. *J Eng Mech-ASCE.* 1994;120(3):593–617.

[58] Bažant ZP, Jirásek M. Nonlocal integral formulations of plasticity and damage: survey of progress. *J Eng Mech-ASCE.* 2002;128(11):1119–1149.

[59] Jirásek M, Marfia S. Non-local damage model based on displacement averaging. *Int J Numer Meth Eng.* 2005;63(1):77–102.

[60] Grassl P, Xenos D, Jirásek M, Horák M. Evaluation of nonlocal approaches for modelling fracture near nonconvex boundaries. *Int J Solids Struct.* 2014;51(18):3239 – 3251.

[61] Suárez F. On the localisation of damage under pure bending using a nonlocal approach. *Int J Solids Struct.* 2018;.

[62] Cervera M, Pelà L, Clemente R, Roca P. A crack-tracking technique for localized damage in quasi-brittle materials. *Eng Fract Mech.* 2010;77(13):2431 – 2450.

[63] Saloustros S, Pelà L, Cervera M. A crack-tracking technique for localized cohesive–frictional damage. *Eng Fract Mech.* 2015;150:96 – 114.

[64] Saloustros S. Tracking localized cracks in the computational analysis of masonry structures. Doctoral Dissertation. Universitat Politècnica de Catalunya; 2017.

Appendix A. Change of base of the tangent tensor

The generalised Hooke law relates the stress and strain tensors by means of the tangent tensor, this relation is valid for any coordinate system; in particular, in the xy and the $\sigma - \tau$ planes it would write:

$$\boldsymbol{\sigma}_{xy} = \boldsymbol{D}_{xy} \cdot \boldsymbol{\varepsilon}_{xy}$$

$$\boldsymbol{\sigma}_{st} = \boldsymbol{D}_{st} \cdot \boldsymbol{\varepsilon}_{st}$$

where subscripts xy and st identify the coordinate system at which each element is expressed.

Following the nomenclature used in Figure 2, the change-of-base matrix $\boldsymbol{L}$ can be expressed as:

$$\boldsymbol{L} = \begin{pmatrix} n_1 & m_1 \\ n_2 & m_2 \end{pmatrix} \tag{20}$$

where subscripts 1 and 2 identify the first and second component of each unit vector.

Then, $\boldsymbol{\sigma}_{xy}$ can be obtained from $\boldsymbol{\sigma}_{st}$ as follows:

$$\boldsymbol{\sigma}_{xy} = \boldsymbol{L} \cdot \boldsymbol{\sigma}_{st} \cdot \boldsymbol{L}^t = \begin{pmatrix} n_1 & m_1 \\ n_2 & m_2 \end{pmatrix} \begin{pmatrix} \sigma_{11} & \sigma_{12} \\ \sigma_{12} & \sigma_{22} \end{pmatrix} \begin{pmatrix} n_1 & n_2 \\ m_1 & m_2 \end{pmatrix} =$$

$$= \begin{pmatrix} n_1 & m_1 \\ n_2 & m_2 \end{pmatrix} \begin{pmatrix} \sigma_{11} n_1 + \sigma_{12} m_1 & \sigma_{11} n_2 + \sigma_{12} m_2 \\ \sigma_{12} n_1 + \sigma_{22} m_1 & \sigma_{12} n_2 + \sigma_{22} m_2 \end{pmatrix} = \cdots =$$

$$= \begin{pmatrix} \sigma_{11} n_1^2 + 2\sigma_{12} m_1 n_1 + \sigma_{22} m_1^2 & \sigma_{11} n_1 n_2 + \sigma_{22} m_1 m_2 + \sigma_{12}(n_1 m_2 + m_1 n_2) \\ \sigma_{11} n_1 n_2 + \sigma_{22} m_1 m_2 + \sigma_{12}(n_1 m_2 + m_1 n_2) & \sigma_{11} n_2^2 + 2\sigma_{12} m_2 n_2 + \sigma_{22} m_2^2 \end{pmatrix}$$

Therefore, the stress tensor components in the xy plane can be expressed in terms of its components in the $\sigma - \tau$ plane in the following matrix form:

$$\begin{pmatrix} \sigma_{xx} \\ \sigma_{yy} \\ \sigma_{xy} \end{pmatrix} = \begin{pmatrix} n_1^2 & m_1^2 & 2m_1 n_1 \\ n_2^2 & m_2^2 & 2m_2 n_2 \\ n_1 n_2 & m_1 m_2 & (n_1 m_2 + m_1 n_2) \end{pmatrix} \begin{pmatrix} \sigma_{11} \\ \sigma_{22} \\ \sigma_{12} \end{pmatrix} \tag{21}$$

The previous matrix will be called $\boldsymbol{A}$.

Following the same procedure, the strain tensor in the xy plane can also be expressed in terms of its components in the $\sigma - \tau$ plane as follows:

$$\begin{pmatrix} \varepsilon_{xx} \\ \varepsilon_{yy} \\ \varepsilon_{xy} \end{pmatrix} = \begin{pmatrix} n_1^2 & m_1^2 & m_1 n_1 \\ n_2^2 & m_2^2 & m_2 n_2 \\ 2n_1 n_2 & 2m_1 m_2 & (n_1 m_2 + m_1 n_2) \end{pmatrix} \begin{pmatrix} \varepsilon_{11} \\ \varepsilon_{22} \\ \varepsilon_{12} \end{pmatrix} \tag{22}$$

This matrix will be referred to as $\boldsymbol{B}$.

Gathering the four previous expressions:

$$\boldsymbol{\sigma}_{xy} = \boldsymbol{D}_{xy} \cdot \boldsymbol{\varepsilon}_{xy} \tag{23}$$

$$\boldsymbol{\sigma}_{st} = \boldsymbol{D}_{st} \cdot \boldsymbol{\varepsilon}_{st} \tag{24}$$

$$\boldsymbol{\sigma}_{xy} = \boldsymbol{A} \cdot \boldsymbol{\sigma}_{st} \tag{25}$$

$$\boldsymbol{\varepsilon}_{xy} = \boldsymbol{B} \cdot \boldsymbol{\varepsilon}_{st} \tag{26}$$

By substituting (24) in (25):

$$\boldsymbol{\sigma}_{xy} = \boldsymbol{A} \cdot \boldsymbol{D}_{st} \cdot \boldsymbol{\varepsilon}_{st} \tag{27}$$

Now, doing the same with (27) and (26) in (23):

$$\boldsymbol{A} \cdot \boldsymbol{D}_{st} \cdot \boldsymbol{\varepsilon}_{st} = \boldsymbol{D}_{xy} \cdot \boldsymbol{B} \cdot \boldsymbol{\varepsilon}_{st}$$

Therefore

$$\boldsymbol{A} \cdot \boldsymbol{D}_{st} = \boldsymbol{D}_{xy} \cdot \boldsymbol{B}$$

So, finally:

$$\boldsymbol{D}_{st} = \boldsymbol{A}^{-1} \cdot \boldsymbol{D}_{xy} \cdot \boldsymbol{B}$$

and:

$$\boldsymbol{D}_{xy} = \boldsymbol{A} \cdot \boldsymbol{D}_{st} \cdot \boldsymbol{B}^{-1}$$